ACS APPLIED MATERIALS & INTERFACES

Research Article

www.acsami.org

Differential Collective- and Single-Cell Behaviors on Silicon Micropillar Arrays

Zeinab Jahed,[†] Ramin Zareian,[†] Yeung Yeung Chau,[‡] Brandon B. Seo,[§] Mary West,[†] Ting Y. Tsui,[§] Weijia Wen,[‡] and Mohammad R. K. Mofrad*[,†,∥]

[†]Molecular Cell Biomechanics Laboratory, Departments of Bioengineering and Mechanical Engineering, University of California—Berkeley, 208A Stanley Hall, Berkeley, California 94720-1762, United States

[∥]Molecular Biophysics and Integrative Bioimaging Division, Lawrence Berkeley National Laboratory, Berkeley, California 94720, United States

[‡]Department of Physics, The Hong Kong University of Science and Technology, Clear Water Bay, Kowloon, Hong Kong, China

[§]Department of Chemical Engineering, University of Waterloo, 200 University Avenue West, Waterloo, Ontario N2L 3G1, Canada

Supporting Information

ABSTRACT: Three-dimensional vertically aligned nano- and micropillars have emerged as promising tools for a variety of biological applications. Despite their increasing usage, the interaction mechanisms of cells with these rigid structures and their effect on single- and collective-cell behaviors are not well understood for different cell types. In the present study, we examine the response of glioma cells to micropillar arrays using a new microfabricated platform consisting of rigid silicon micropillar arrays of various shapes, sizes, and configurations fabricated on a single platform. We compare collective- and single-cell behaviors at micropillar array interfaces and show that glial cells under identical chemical conditions form distinct arrangements on arrays of different shapes and sizes. Tumor-like aggregation and branching of glial cells only occur on arrays with feature diameters greater than 2 μm, and distinct transitions are observed at interfaces between various arrays on the platform. Additionally, despite the same side-to-side spacing and gaps between micropillars, single glial cells interact with the flat silicon surface in the gap between small pillars but sit on top of larger micropillars. Furthermore, micropillars induced local changes in stress fibers and actin-rich filopodia protrusions as the cells conformed to the shape of spatial cues formed by these micropillars.

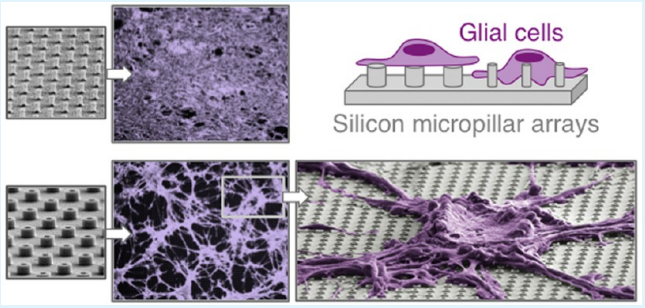

KEYWORDS: *glioma, glioblastoma, cell nanopillar, cell micropillar, nanowire, topography sensing, cell adhesion, mechanotransduction*

INTRODUCTION

Cells have the ability to sense and respond to the micro- and nanoscale topography of their environment.[1] Studies on micro- and nanopatterned engineered surfaces have demonstrated the influence of topography on a variety of cellular functions including the directed migration of endothelial cells and fibroblasts,[2,3] osteogenic differentiation of stem cells,[4−7] altered mechanosensitive gene expressions in fibroblasts,[8−11] directional polarization of neurons,[12−17] and immobilization of tumor cells.[18,19]

Researchers have taken advantage of these cellular responses and utilized micro- and nanostructured surfaces, in particular vertically aligned three-dimensional (3D) pillar structures, for a wide range of biological applications. Small-diameter nanowires with high aspect ratios are known to penetrate the cell membrane and are therefore most commonly used for applications requiring intracellular access such as drug delivery.[20−25] On the other hand, larger pillar structures are engulfed by the cell without membrane rupture and are more commonly used in applications requiring an intact cell membrane. For example, nanopillar arrays have been used for noninvasive immobilization of neurons to obtain long periods of activity measurements from the same neuron.[26] Furthermore, silicon micropillar arrays have been utilized for the efficient isolation and capture of circulating tumor cells, possibly through enhanced local topographic interactions of cells with the micropillars.[18,19,27,28]

A great number of experimental and computational studies have examined the mechanisms of small-diameter nanowire penetration into cells, showing that penetration depends on several parameters including the nanowire diameter, height-to-diameter aspect ratio, and spacing.[23,29−32] However, a limited number of studies have looked at cell interactions with larger pillar structures, where penetration is unlikely to occur.[18,33,34]

Received: July 17, 2016
Accepted: August 18, 2016
Published: August 18, 2016

DOI: 10.1021/acsami.6b08668
ACS Appl. Mater. Interfaces 2016, 8, 23604−23613

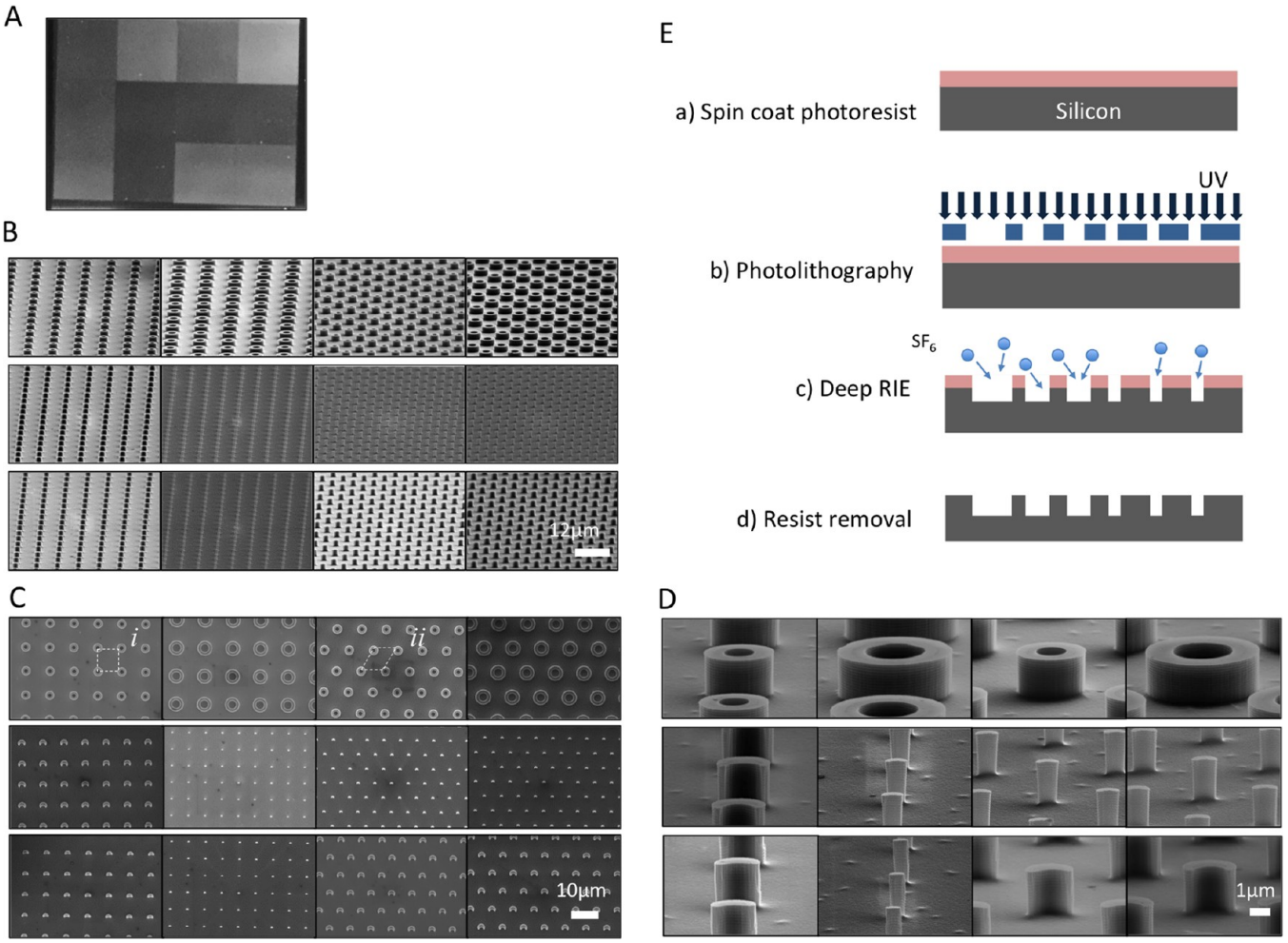

Figure 1. Fabricated silicon platform consisting of micropillar arrays of various shape, sizes, and configurations. (A) Digital camera image of the silicon platform showing 12 different micropillar arrays fabricated on a single device. (B) SEM micrograph of each array observed at 70° and (C) 0° stage tilt angles. (D) High-magnification SEM micrograph of each micropillar in the arrays. (E) Fabrication process of a silicon micropillar platform including the spin coating of a photoresist onto silicon substrates (a), photolithography to achieve the desired patterns on the resists (b), followed by a deep reactive ion-etching process in which the silicon micropillars are fabricated (c), and a final removal of the photoresist (d).

Wang et al. examined the role of spacing and diameter on the capture rates of circulating tumor cells and showed that higher capture rates were achievable on pillar arrays of smaller diameters compared with larger pillars or a flat silicon wafer.[18] Hanson et al. characterized the cell−nanopillar interface using transmission electron microscopy and showed that cortical neurons preferentially sit on top of nanopillars with 500 nm diameters and 1 μm center-to-center spacing but engulf nanopillars with 200 nm diameters and similar center-to-center spacing.[33] Finally, Xie et al. developed a continuum mechanical model to quantify the cell−pillar interactions and showed that this interaction is dependent on not only the pillar geometry but also the flat surface or gap available between the nanopillars, which is a function of nanopillar spacing. Their results suggest that decreased nanopillar spacing can lift the cells away from the flat silicon surface. Despite great advancements in understanding cell−pillar interactions, the effects of these rigid structures on intracellular components such as the nucleus and cytoskeleton remain understudied. Additionally, the collective behaviors of cells on pillar arrays are poorly understood. In this study, we fabricated vertically aligned arrays of micropillar structures side by side on a silicon platform. These micropillar arrays consisted of micropillars of identical heights and side-to-side spacings but with varying geometries, allowing us to explore single- and collective-cell behaviors at array interfaces. Using high-resolution scanning electron microscopy (SEM) and fluorescent microscopy techniques, we show that cells on the same platform interact distinctly with micropillars of varying sizes. Interestingly, aggregation and branching of cells was observed on specific micropillar arrays but restrained on neighboring arrays with different micropillar geometries. Cells interacted with the top surfaces of larger micropillar arrays and conversely with the side walls and flat areas between smaller-diameter micropillars. Furthermore, cell protrusions conformed to the shape of the micropillars, and local cytoskeletal rearrangements were observed on micropillar arrays.

RESULTS

Fabrication of Silicon Platform. Arrays of rigid silicon micropillars of various geometries were successfully fabricated side by side on a silicon platform (Figure 1A). This platform was used to assess glioma cell responses to vertically aligned 3D micropillars of varying geometry and configuration. Fabricated micropillars were characterized using SEM, as shown in Figure 1B−D. The outer diameters of the fabricated micropillars were

DOI: 10.1021/acsami.6b08668
ACS Appl. Mater. Interfaces 2016, 8, 23604−23613

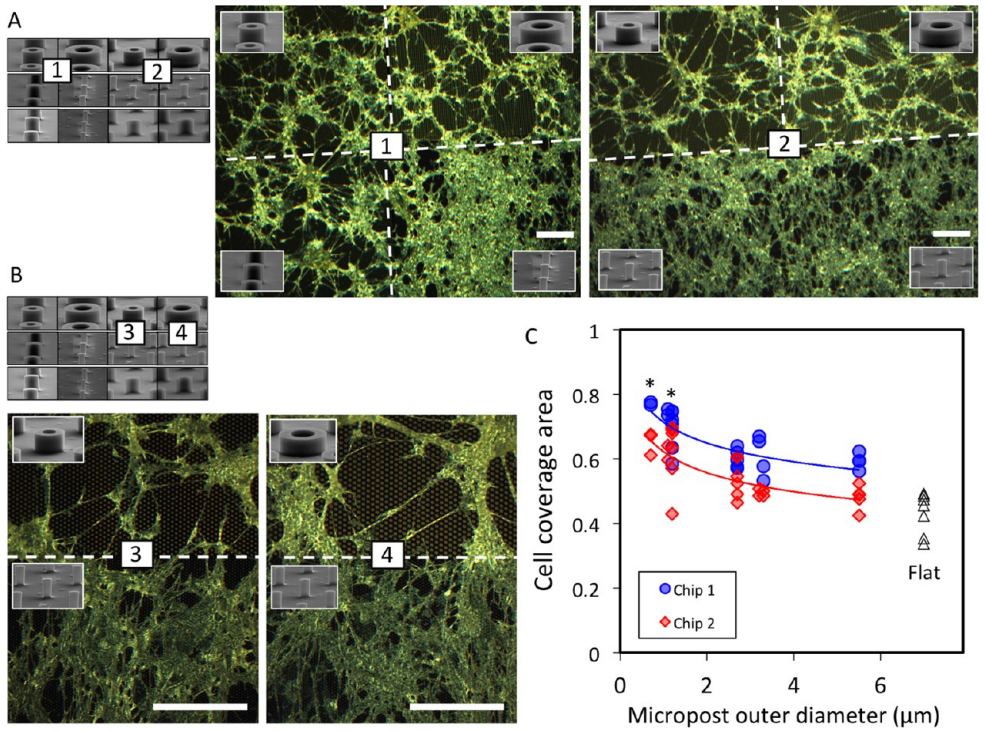

Figure 2. (A) Dark-field microscopy images of U87 glioma cells on a silicon micropillar platform showing the interfaces between the smallest and largest micropillars. Cell arrangements and branching are evidently different between the various regions. (B) High-magnification dark-field microscopy image of U87 cells spreading differentially on various regions of the micropillar platform. (C) Cell coverage area as a function of the micropillar size. The asterisk symbols represent the differences compared with all other micropillars with outer diameters greater than 2 μm and the control flat silicon substrate (Mann−Whitney U test; $p < 0.01$). Scale bars represent 200 μm.

measured to range from 0.7 to 5.5 μm. Each silicon platform consisted of two arrays of the same micropillar geometry, one with a square configuration (Figure 1C-i) and another with a hexagonal configuration (Figure 1C-ii). In all arrays, a constant 5 μm side-to-side spacing was maintained between neighboring micropillars, resulting in comparable free flat areas between the micropillars irrespective of their sizes. Furthermore, the heights of all micropillars were maintained at 2 μm. The designed platform allowed for the characterization of single glioma interactions with the distinct topographic features of each micropillar array, comparison of cell behaviors at array interfaces, and assessment of the collective behaviors of cells on the entire silicon platform.

Preferential Aggregation of Cells on Large Micropillar Arrays. U87 glioma cells were plated on the silicon platforms uniformly covering all micropillar arrays. After 24 h, cells showed a slightly higher concentration on small-sized micropillars (Figure S1). Interestingly, after 68 h, glioma cells exhibited distinctive arrangements on various micropillar arrays. Cells formed aggregates on micropillars with outer diameters larger than 2 μm, whereas cells on micropillars smaller than 2 μm were evenly distributed on the platform, leaving small voids. This was evident from dark-field microscopy images of the interfaces between small (<2 μm) and large (>2 μm) micropillar arrays on both square (Figure 2A-1) and hexagonal (Figure 2A-2) array configurations on the silicon platforms. Magnified images indicated larger voids (areas with no cells) and longer branchlike connections between cell aggregates on larger micropillar arrays, as shown in Figure 2B. These results were observed on several silicon platforms, and to quantify this collective-cell behavior, we measured the cell coverage area, defined as the ratio between the area covered by cells and the total imaged area (see the Methods section), for each micropillar array on two identical silicon platforms, as shown in Figure 2C (blue and red curves). Both platforms showed similar trends in coverage area as a function of the micropillar diameter. In both cases, micropillars with diameters <2 μm showed the highest cell coverage and a decrease in the cell coverage area for larger micropillars (Figure 2C). The lowest coverage areas were observed for cells on a smooth flat silicon substrate (Figure 2C). As shown in Figure 3, although platform 1 (blue) and platform 2 (red) show the same trends, platform 1 (blue curve) exhibited overall higher cell coverages on all micropillar arrays despite identical cell seeding and growth conditions. Therefore, for better control, in this study we only compare the cell behaviors on different micropillar arrays of the same silicon platform.

The highest cell coverage areas were observed within the smaller silicon micropillar dimensions with outer diameters of <2 μm and were statistically significant from all other micropillars with outer diameters >2 μm and from a control flat silicon substrate. However, the differences between the measured coverage areas of micropillar arrays with outer diameters ranging from 2.5 to 5.5 μm were not statistically significant.

We also compared the cell coverage areas for square versus hexagonal configurations of each micropillar size for both platforms, as shown in Figure S2. However, the coverage areas seem to be independent of the micropillar configurations tested in this study.

In order to observe cell−micropillar interactions in 3D, the silicon platforms were inspected using high-resolution SEM at a 70° stage tilt at the mircopillar array interfaces. On larger structures, glioma cells formed large cell aggregates with long

DOI: 10.1021/acsami.6b08668
ACS Appl. Mater. Interfaces 2016, 8, 23604−23613

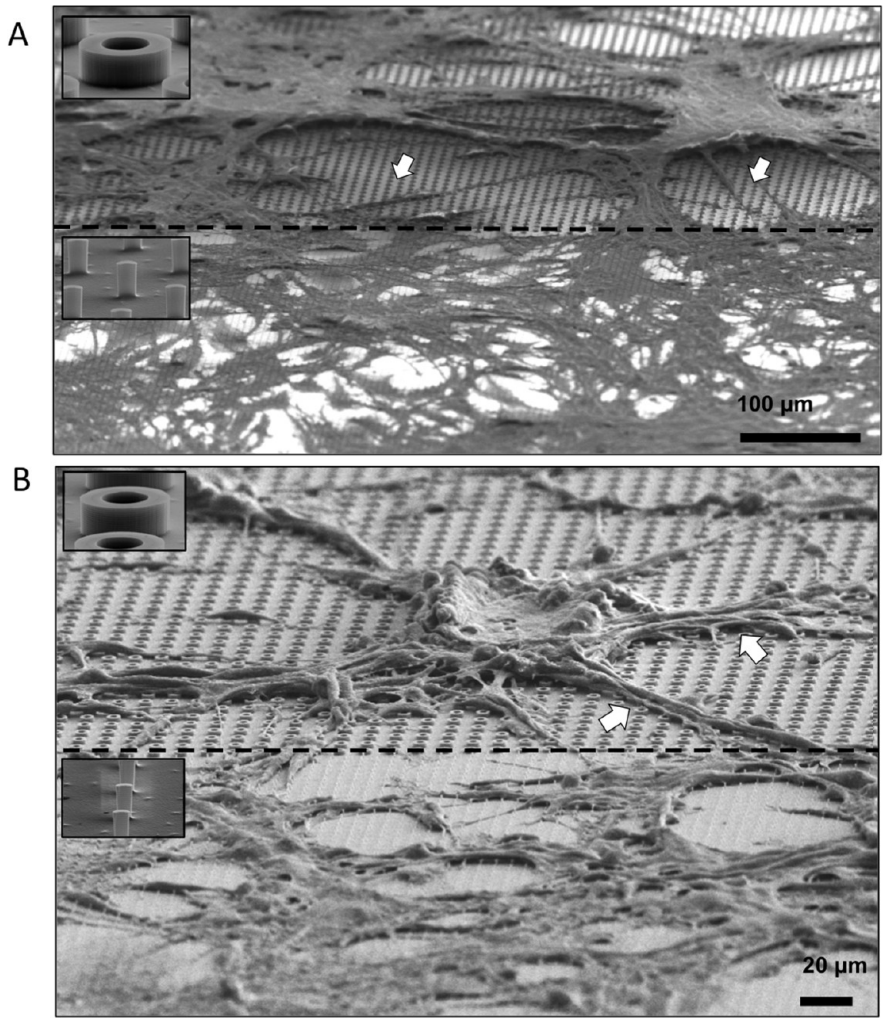

Figure 3. SEM micrograph of U87 glioma cells on the interface of two micropillar arrays with different sizes, with (A) hexagonal or (B) square configurations. Cells show a tendency to form tumor-like aggregates on larger structures (top), whereas fewer clusters are seen on small micropillars (bottom). These aggregates are connected via long branches consisting of one or several cells (white arrows).

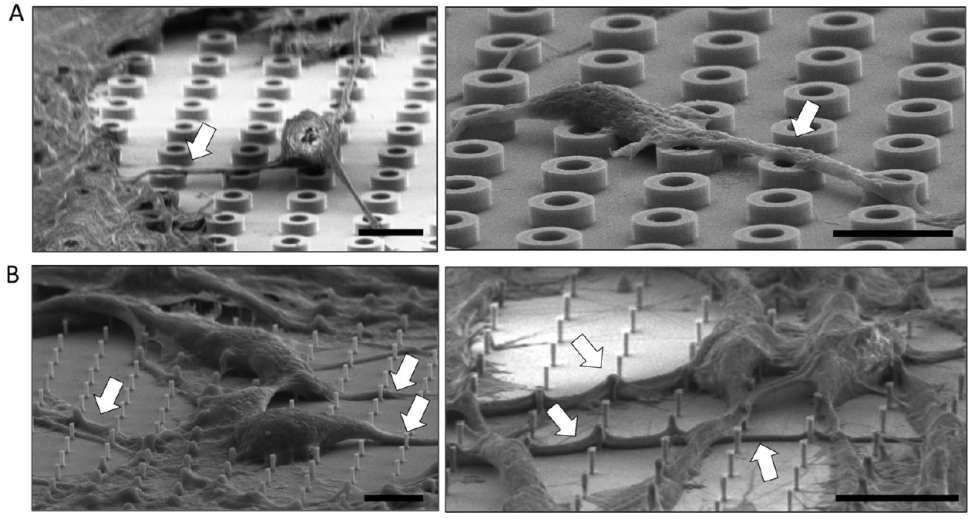

Figure 4. Representative images of U87 glioma–micropillar interactions. (A) U87 cells sit on top of micropillars with outer diameters >2 μm, while cell protrusions (white arrows) interact with pillar tops rather than the flat area in the gap between micropillars. (B) U87 glioma cells and their protrusions (white arrows) interact with small micropillars (outer diameters <2 μm) as well as the flat silicon area between micropillars. All scale bars correspond to 10 μm.

DOI: 10.1021/acsami.6b08668
ACS Appl. Mater. Interfaces 2016, 8, 23604–23613

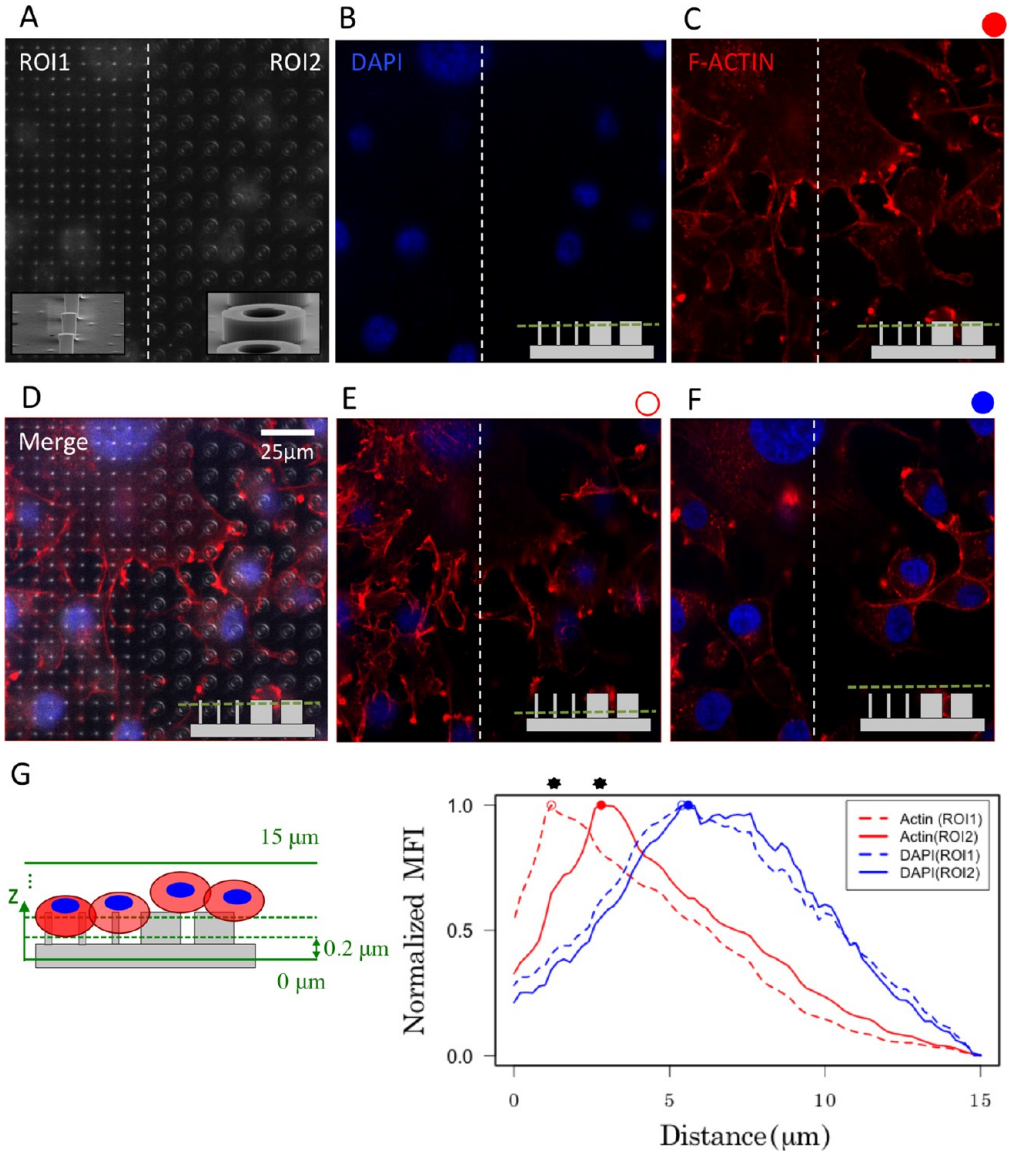

Figure 5. (A) Optical image of U87 cells on interfaces between small (ROI1) and large (ROI2) micropillars. (B) Confocal image of cell nuclei stained with blue (DAPI) and (C) the actin cytoskeleton with red (F-actin) on ROI1 and ROI2. (D) Overlay of optical and confocal images to show the relative positions of the cells on the two ROIs. (E) Confocal plane with a maximum DAPI fluorescent intensity for ROI2. (F) Confocal plane with a maximum F-actin fluorescent intensity for ROI1. (G) Normalized MFI of F-actin and DAPI for ROI1 and ROI2 as a function of the distance from the initial confocal plane on the flat surface. The schematic on the left shows the confocal z-slices from 0 to 15 at 0.2 μm intervals. The z-slice with a maximum F-actin intensity is shown with a hollow red circle for ROI1 and with a filled red circle for ROI2.

branches consisting of few elongated cells connecting neighboring cell aggregates in both the hexagonal (Figure 3A) and square (Figure 3B) array configurations. These SEM images also confirmed the presence of larger voids between cell aggregates on large micropillar arrays.

F-Actin-Rich Cell Protrusions That Interact Distinctly with Small versus Large Micropillars. High-resolution SEM inspections of single cell−micropillar interactions showed that despite similar side-to-side spacing between micropillars of all sizes, on large micropillars (>2 μm), the cell body is lifted away from the flat silicon substrate and cells preferentially anchor onto micropillar tops, as opposed to the flat silicon regions between the micropillars (Figure 4A). Contrarily, on smaller micropillars (<2 μm), the cell body was close to the flat silicon substrate and cell protrusions extended between these micropillars (Figure 4B).

We next used 3D confocal z-stacks to compare F-actin and 4′,6-diamidino-2-phenylindole (DAPI) expressions at various focal planes above the silicon platform at interfaces between small (Figure 5A-ROI1) and large (Figure 5A-ROI2) micropillars. To analyze single cell−micropillar interactions and avoid cell aggregation, cells used for confocal microscopy were plated on the silicon substrate for 3 h. A representative z-slice near the top of the micropillars is shown in Figure 5B,C,D. A higher number of F-actin-rich protrusions with high-intensity F-actin expressions are observable on micropillar tops in ROI2, compared to ROI1 in the z-slice shown (Figure 5C). Conversely, cells in ROI1 show higher F-actin-rich protrusions at a lower z-slice, as shown in Figure 5E. Normalized mean fluorescent intensities (MFIs) for F-actin in ROI1 peaked at a slice ∼1.8 μm lower than ROI2 (Figure 5G). This difference is approximately equivalent to the height of the micropillars,

DOI: 10.1021/acsami.6b08668
ACS Appl. Mater. Interfaces 2016, 8, 23604−23613

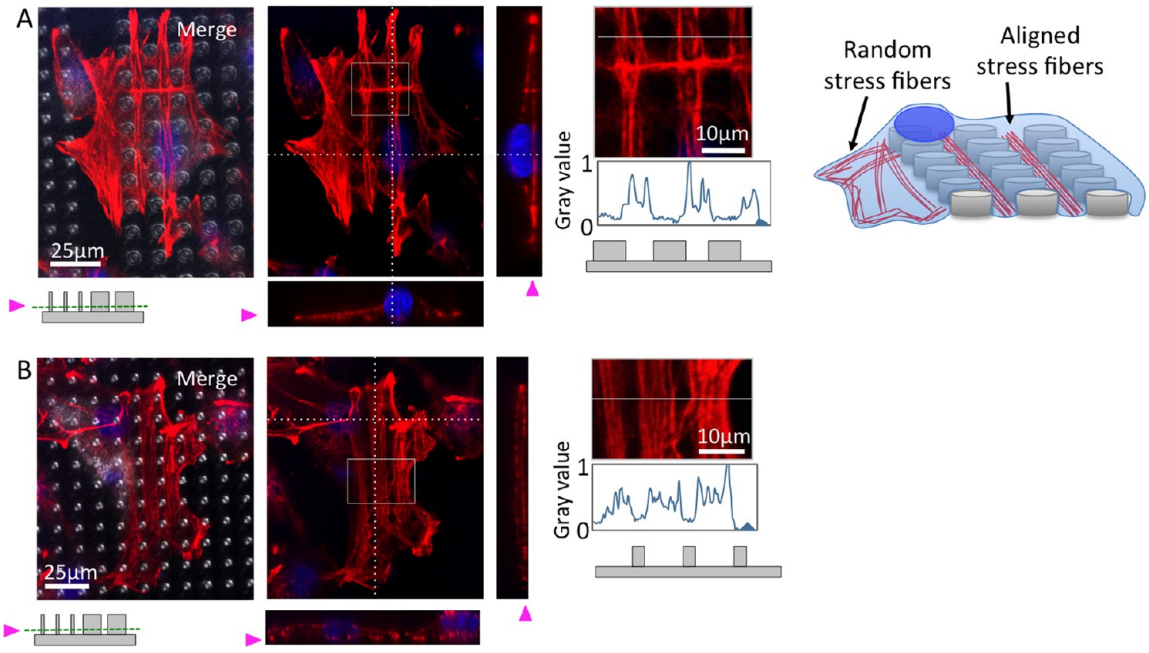

Figure 6. (A) Confocal z-stacks showing localized, elongated, and aligned vertical and horizontal stress fibers in response to spatial limitations formed in the gaps between the micropillars on 5.5 μm hollow-shaped micropillars with square configurations. (B) Elongated and aligned actin stress fibers on 3.2 μm hollow micropillar arrays with square configurations.

suggesting that cells in ROI2 interact and explore the micropillar tops with actin-rich extensions, whereas cells in ROI1 interact mostly with the bottom of the micropillars and the flat regions between the micropillars. Instead, normalized MFIs for DAPI showed peaks at a distance several microns above the micropillars on both ROIs (Figure 5C,G), suggesting that cell nuclei are positioned above the micropillars in both ROIs. The z-slice with a maximum normalized MFI for DAPI is shown in Figure 5F.

Local Cytoskeletal Rearrangements in Response to a Micropillar Geometry. The cytoskeletal arrangements of fully spread glioma cells on various micropillar arrays were also examined through confocal microscopy. On 5.5 μm hollow-shaped micropillars with square configurations, cells exhibited remarkable localized stress fibers aligned along free spaces between micropillars. The cell shown in Figure 6A exhibited localized, elongated, and aligned vertical and horizontal stress fibers in response to spatial limitations formed between the micropillars, whereas stress fibers were arranged randomly on parts of the cell that rested on the free space between two arrays lacking spatial cues. Orthogonal views of the z-stacks also indicate the nuclei positioned on top of the micropillars in these cells. These elongated and aligned actin stress fibers were also observable on 3.2 μm hollow micropillar arrays with square configurations, as shown in Figure 6B. The dark areas free of F-actin between the elongated stress fibers correspond to the location of the micropillars, as is evident from the merged images in Figure 6A,B. The F-actin fluorescent intensity profiles along lines crossing these micropillars also show that the drops in intensity correspond to the location of the micropillars. A similar phenomenon was observed on hexagonal array configurations; however, the actin stress fibers of cells on these arrays were aligned diagonally at random orientations (Figure S3), suggesting that these cells rearrange their cytoskeleton to conform to the micropillar array shape.

F-actin-rich cell protrusions also traveled inside the openings of hollow micropillars, as is evident from the SEM images shown in Figure 7A. Confocal microscopy revealed circular and high-intensity F-actin expressions on hollow micropillars with hole diameters of 1.8−5 μm. Furthermore, actin-rich filopodia conformed to the sharp edges on top of hollow micropillars (Figure 7C), where high expressions of F-actin are observable at filopodia tips.

DISCUSSION

Vertically aligned micropillars of solid and hollow cross sections are used for a variety of biological applications including tumor-cell capture,[19,35] drug delivery into cells,[20,25] and the recording of neuronal activities.[26,36−38] In this study, a silicon platform was developed and used to explore the responses of glioma cells to silicon micropillar arrays of various sizes. The silicon micropillars used in this study were rigid: i.e., cells were not able to deform these micropillars. Therefore, we assume a constant stiffness for all micropillars arrays, eliminating the role of stiffness in the differential responses that we observed. Indeed, glioma cells also show sensitivity to substrate stiffness, and their response has been characterized by several groups.[39−41] Furthermore, micropillars of various sizes were fabricated side by side on silicon platforms, providing identical chemical environments for the cells. Thereby, the distinguishable collective- and single-cell behaviors exhibited by glioma cells on various micropillar arrays were attributed to their differential responses to the size of the micropillars.

Previous studies have looked at the effect of the pillar size and spacing on the cell−pillar interfaces by using the same center-to-center spacing but varying the pillar sizes. However, using the same center-to-center spacing results in smaller flat surfaces available to the cells between larger pillars compared with smaller pillars. Hence, in this study, instead of center-to-center distances, we kept the side-to-side spacing (i.e., gap) of the pillars constant while changing the pillar sizes. Xie et al.

DOI: 10.1021/acsami.6b08668
ACS Appl. Mater. Interfaces 2016, 8, 23604−23613

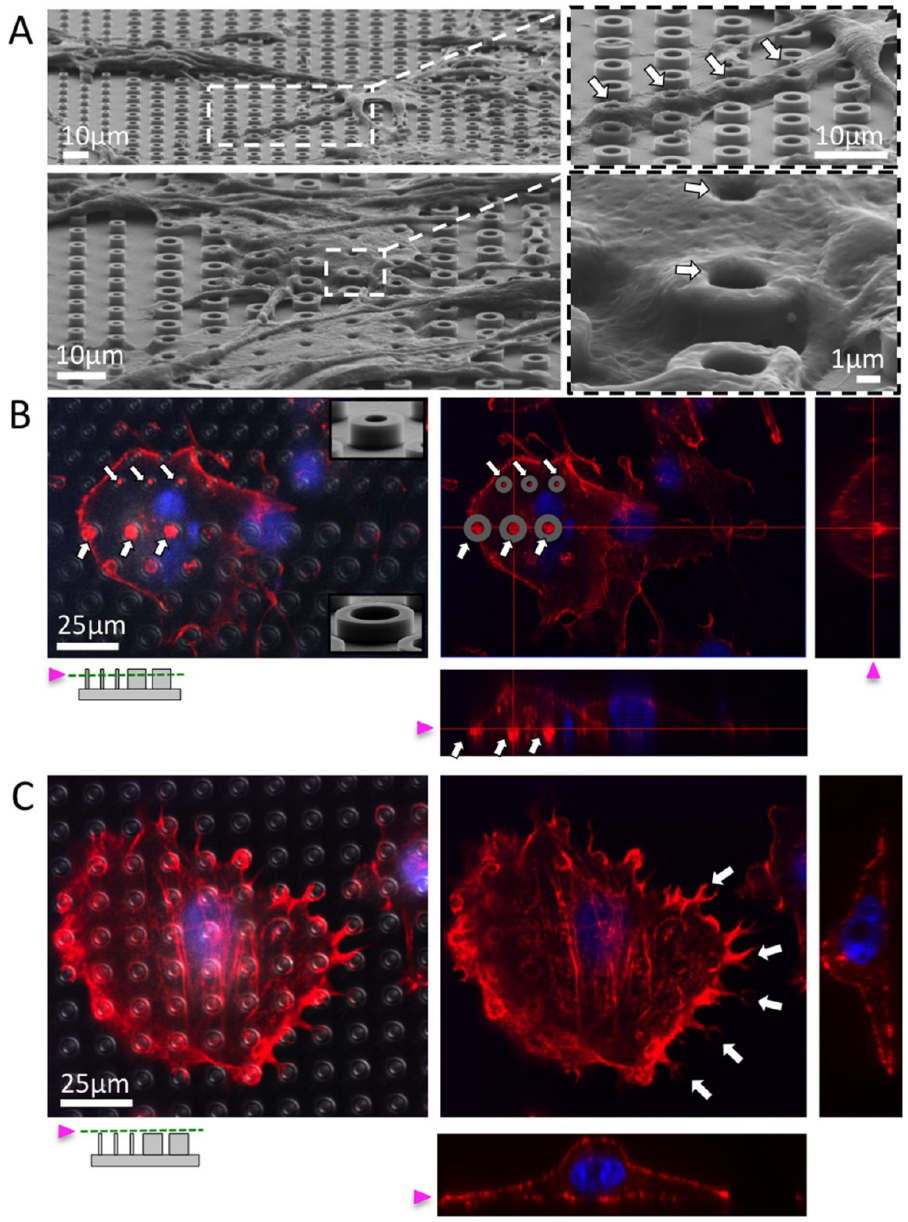

Figure 7. (A) SEM micrograph of U87 cells protruding into hollow-shaped micropillars, (B) Confocal images indicating the high expression of F-actin within the openings of hollow micropillars (arrows). (C) Confocal z-stack of a cell on top of micropillars showing actin-rich protrusions conformed to the shape of hollow micropillars, with high F-actin expressions on sharp edges.

observed that Chinese hamster ovary cells were able to deform and wrap around pillars of 5 μm spacing and made contact with the flat substrate between the pillars. On the other hand, these cells were lifted away from the substrate on pillars with the same size but with a reduced spacing of 2 μm.[29] Here, we show that, despite the 5 μm side-to-side spacing of all arrays, whether glial cells make contact with the flat substrate depends highly on the pillar size (Figure 8). Even with similar flat surface areas available to the cell between micropillars of different sizes, glioma cells preferentially interacted with the tops and sides of large micropillars rather than the flat surface between pillars. This was evident from both high-resolution SEM inspections (Figure 4A,B) and confocal z-stacks showing F-actin expressions at different planes at micropillar array interfaces (Figure 7).

The preferential interactions of cells with micropillar tops for larger arrays (>2 μm) may be attributed to the higher surface area provided by these structures for cells to anchor onto. After landing on these pillars, cells can form adhesions on the micropillar tops, as depicted in Figure 8A. Subsequently, in order to strengthen their anchorage, glioma cells explore the nearby microenvironment through actin-rich protrusions (as seen in Figure 7C) and spread on top of multiple micropillars while forming adhesions on the tops and sidewalls of these micropillars (Figure 8A). Conversely, smaller (<2 μm) micropillars do not provide enough anchorage area for the cells on their top surfaces, resulting in cells deforming around these pillars to anchor onto the flat silicon area (Figure 8B). Therefore, cells form strong adhesions on the flat areas as well as the micropillar sidewalls and tightly wrap around these micropillars. Note that the same flat area is available to cells in the gaps between large micropillar arrays, but cells do not deform around the pillars to reach this flat gap area on large micropillars. The deformation of cells around small micropillars

DOI: 10.1021/acsami.6b08668
ACS Appl. Mater. Interfaces 2016, 8, 23604−23613

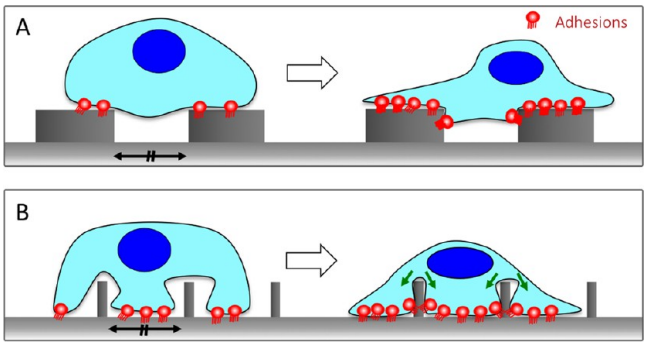

Figure 8. Hypothetical model of cell−micropillar interactions: (A) Micropillars with outer diameters of greater than 2 μm, with a side-to-side spacing of 5 μm, provide enough anchorage area for glioma cells to form adhesions on top of these pillars. Subsequent to initial attachments, cells spread on top of these pillars and away from the flat silicon substrate between pillars while anchoring to the pillar tops and sides. (B) Micropillars with outer diameters of less than 2 μm and a side-to-side spacing of 5 μm do not provide enough anchorage area for cells, resulting in cell deformation around these pillars and interaction with the available flat space between micropillars. Subsequently, cells spread on these micropillars, wrapping tightly around the micropillars and forming strong adhesions on the flat silicon substrate as well as micropillar sidewalls. Black arrows indicate the equal side-to-side spacing between micropillars of different sizes.

to form 2D adhesions on both the flat silicon surface and the sidewalls of small micropillars could lead to the trapping and immobilization of cells on these surfaces. Immobilization of cells on nanopillar arrays was demonstrated previously for circulating tumor cells,[18,19] neurons,[26] and mouse fibroblasts.[42] Glioma cells with reduced motility may be unable to form aggregates on the small micropillar arrays used in this study, which would explain their differential arrangements on top of small micropillar arrays; however, further live cell imaging would be required to verify a reduction in the cell motility on small micropillar arrays. Our future studies will aim at conducting live cell imaging and comparing cell migration speeds on various micropillar arrays. We also showed that the stresses induced in the cell body to conform to the shape of its underlying substrate also resulted in local changes in the cytoskeletal organization and F-actin expression for the glial cells on our silicon platforms (Figures 6 and 7). The long-term effects of such changes on cell behaviors remain unknown.

CONCLUSIONS AND FUTURE PERSPECTIVES

Our results demonstrated the significance of the micropillar size on collective- and single-glioma behaviors. The size of the silicon micropillars determined the arrangement of the glioma cells on these structures: cells formed small tumor-like clusters on larger micropillars but were evenly spread out on small micropillars. Interestingly, we did not observe such distinct cell arrangements for PC3 cancer cells or 3T3 mouse fibroblasts on the same silicon substrate (unpublished work); this is not unexpected because the response of the cells to the size of the micropillars and spacing is, in part, dependent on the cell size, shape, and stiffness.[29] Other cell types may show similar behaviors on smaller or larger micropillars than the ones used in this study depending on their cell shape and properties such as stiffness. Additionally, glioma cells are specifically known to be sensitive to the shape of their microenvironment in the brain. In fact, brain tumor progression is regulated by the transduction of particular physical and chemical signals in the brain extracellular environment.[43] Specifically, glioma cell growth and invasion rely on the detection of specific topographic patterns in brain tissue.[43−47] Further studies aimed at understanding the mechanisms of cell sensitivity to micropillar shape and size not only will allow the design and tuning of micropillar platforms based on their desired applications but may additionally provide insight into the in vivo shape-sensing mechanisms of glioma cells.

METHODS

Silicon Micropillar Platform Fabrication Process. A total of 12 different arrays of silicon micropillars were fabricated side by side. These arrays consisted of large micropillars with hollow cross-sectional geometries or small C-shaped micropillars. Hollow micropillars were fabricated with inner diameters of 1.5, 2, 3, and 5 μm, all with a wall thickness of 1.5 μm, and a side-to-side spacing of 5 μm, arranged in both square and hexagonal configurations. For the smaller C-shaped micropillars, the final measured circle diameters are 1.5 and 3 μm, with openings of 0.5 and 0.75 μm on the edges of the micropillars, with a side-to-side spacing of 5 μm, arranged in both square and hexagonal configurations. Each micropillar array covered an area of approximately 3.5 × 3.5 mm.

After a clean silicon wafer coated with a photoresist (AZ 7908) was soft-baked, it underwent UV exposure in an ASML Stepper 5000 (PHT-S1); after development of the patterns, followed by hard-baking, we used deep reactive ion etching (Surface Technology Systems, ICP DRIE) to render micropillars with a height of 2 μm.

The undulating sidewalls were created by pulsed etching in a typical Bosch process. C4F8 of 15 Sccm and Sf6 of 45 and 5 Sccm were used during etching, and 75 Sccm of C4F8 was used in the passivation process.

Cell Culture. U-87 cells (Human Primary Glioblastoma cell line) were provided from the Department of Molecular and Cell Biology at the University of California—Berkeley. Cells were cultured in cell DMEM 1X, Dulbecco's modified Eagle medium (with 4.5 g/L glucose, L-glutamine, and sodium pyruvate, Corning Cellgro). The cell DMEM 1X was enriched with 10% fetal bovine serum (Corning Cellgro), 1% penicillin−streptomycin (Corning Cellgro), and 1% nonessential amino acid (Gibco, Life Technologies). Cells were cultured and kept in an incubator, which was set to 5% CO_2 and 37 °C temperature. In this study, cells were passaged every week with a passage number between 15 and 30 for all experiments. For each experiment, cells were washed one time with PBS 1X (phosphate-buffered saline, Corning) and trypsinized by 0.05% preheated Trypsin (0.53 mM ethyl-enediaminetetraacetic acid, 1X without sodium bicarbonate, Corning) for 5 min in a laminar hood and incubator. Then, cells were collected in 15 mL centrifuge tubes and centrifuged at 850 rpm for 5 min. At the end of the preparation of the cell solution, the cell concentration was adjusted to 16 × 10^4 cells/mL for all experiments in this study.

Seeding U-87 Cells on Silicon Platforms. All silicon micropillar platforms were placed onto sterile six-well cell culture plates (flat bottom with a lid, Corning) and submerged in 70% ethanol for 5 min in a laminar hood. After treatment with ethanol, all platforms were washed three times with PBS 1X and once more using the enriched cell culture DMEM 1X. Then, cells were seeded on the sterilized micropillar platforms at a concentration of 16 × 10^4 cells/mL. Silicon platforms were then placed in new six-well culture plates, 3 mL of the prepared cell solution (16 × 10^4 cells/mL) was added to each well, and the plates were kept in an incubator. Every 24 h, cells were fed fresh enriched cell culture DMEM throughout the experiments.

Cell Imaging and Analysis. *Confocal Microscopy.* Cells were washed and fixed with 4% parafalmadehyde. Membranes were permeabilized with 5% goat serum and 1% triton-X in PBS. Cells were then stained for F-actin and DNA with Pahlloidin and DAPI, respectively. Swept-field confocal microscopy was conducted using a Bruker/Prairie Aurora launch microscope system. Confocal z-stacks were taken using a 60× water-dipping objective (LUMPlan Fl, NA = XX, Olympus) at either 200 or 300 nm z-steps using a 35 μm pinhole aperture setting. Images (512 × 512) were taken using an EM-CCD

DOI: 10.1021/acsami.6b08668
ACS Appl. Mater. Interfaces 2016, 8, 23604−23613

camera. Images were additionally taken using transmitted light to superimpose on the fluorescent images.

SEM Procedure. To prepare cells for electron microscopy, samples were rinsed with 0.2 mM sodium phosphate buffer (v/v: 36 mL Na_2HPO_4/14 mL NaH_2PO_4) and then fixed with 2.5% glutaraldehyde at 4 °C overnight. Samples were then dehydrated using a graded series of ethanol dilutions (10−100%), dried, and coated with a ∼10 nm layer of gold prior to microscopy.

Coverage Area Calculations. The cell coverage area was simply defined as the ratio between the area covered by cells or its protrusions and the bare silicon area. In order to measure the cell coverage area of each array, micrographs were converted to binary images and quantified using *ImageJ*. For each measured cell coverage area value, a two-tailed Mann−Whitney test was performed to conclude that the difference observed between the groups for the measured cell coverage area is unlikely to have occurred by chance at both 0.05 and 0.01 significance levels.

■ ASSOCIATED CONTENT

Supporting Information

The Supporting Information is available free of charge on the ACS Publications website at DOI: 10.1021/acsami.6b08668.

Cell coverage after 24 h (Figure S1), cell coverage data for hexagonal versus square micropillar configurations (Figure S2), and stress fiber orientation on hexagonal micropillars (Figure S3) (PDF)

■ AUTHOR INFORMATION

Corresponding Author

*Phone: 510-643-8165. E-mail: mofrad@berkeley.edu.

Notes

The authors declare no competing financial interest.

■ ACKNOWLEDGMENTS

This work was supported by grants from the National Science Foundation (CAREER Award CBET-0955291 to M.R.K.M.) and the Natural Sciences and Engineering Research Council of Canada (to Z.J.) and an AHA postdoctoral fellowship (to R.Z.).

■ REFERENCES

(1) Kim, D. H.; Provenzano, P. P.; Smith, C. L.; Levchenko, A. Matrix Nanotopography as a Regulator of Cell Function. *J. Cell Biol.* **2012**, *197* (3), 351−360.

(2) Jiang, X.; Bruzewicz, D. a; Wong, A. P.; Piel, M.; Whitesides, G. M. Directing Cell Migration with Asymmetric Micropatterns. *Proc. Natl. Acad. Sci. U. S. A.* **2005**, *102* (4), 975−978.

(3) Mahmud, G.; Campbell, C. J.; Bishop, K. J. M.; Komarova, Y. a.; Chaga, O.; Soh, S.; Huda, S.; Kandere-Grzybowska, K.; Grzybowski, B. a. Directing Cell Motions on Micropatterned Ratchets. *Nat. Phys.* **2009**, *5* (8), 606−612.

(4) McBeath, R.; Pirone, D. M.; Nelson, C. M.; Bhadriraju, K.; Chen, C. S. Cell Shape, Cytoskeletal Tension, and RhoA Regulate Stem Cell Lineage Commitment. *Dev. Cell* **2004**, *6* (4), 483−495.

(5) Avizienyte, E.; Frame, M. C. Src and FAK Signalling Controls Adhesion Fate and the Epithelial-to-Mesenchymal Transition. *Curr. Opin. Cell Biol.* **2005**, *17* (5), 542−547.

(6) Popat, K. C.; Chatvanichkul, K.-I.; Barnes, G. L.; Latempa, T. J.; Grimes, C. A.; Desai, T. A. Osteogenic Differentiation of Marrow Stromal Cells Cultured on Nanoporous Alumni Surfaces. *J. Biomed. Mater. Res., Part A* **2007**, *80A* (4), 955−964.

(7) Gittens, R. A.; Olivares-Navarrete, R.; McLachlan, T.; Cai, Y.; Hyzy, S. L.; Schneider, J. M.; Schwartz, Z.; Sandhage, K. H.; Boyan, B. D. Differential Responses of Osteoblast Lineage Cells to Nanotopographically-Modified, Microroughened Titanium- Aluminum-Vanadium Alloy Surfaces. *Biomaterials* **2012**, *33* (35), 8986−8994.

(8) McNamara, L. E.; Burchmore, R.; Riehle, M. O.; Herzyk, P.; Biggs, M. J. P.; Wilkinson, C. D. W.; Curtis, A. S. G.; Dalby, M. J. The Role of Microtopography in Cellular Mechanotransduction. *Biomaterials* **2012**, *33* (10), 2835−2847.

(9) Dalby, M. J.; Gadegaard, N.; Riehle, M. O.; Wilkinson, C. D. W.; Curtis, A. S. G. Investigating Filopodia Sensing Using Arrays of Defined Nano-Pits down to 35 Nm Diameter in Size. *Int. J. Biochem. Cell Biol.* **2004**, *36* (10), 2005−2015.

(10) Dalby, M. J.; Riehle, M. O.; Sutherland, D. S.; Agheli, H.; Curtis, A. S. G. Use of Nanotopography to Study Mechanotransduction in Fibroblasts–Methods and Perspectives. *Eur. J. Cell Biol.* **2004**, *83* (4), 159−169.

(11) Dalby, M. J. Topographically Induced Direct Cell Mechanotransduction. *Med. Eng. Phys.* **2005**, *27* (9), 730−742.

(12) Rajnicek, a; Britland, S.; McCaig, C. Contact Guidance of CNS Neurites on Grooved Quartz: Influence of Groove Dimensions, Neuronal Age and Cell Type. *J. Cell Sci.* **1997**, *110*, 2905−2913.

(13) Fozdar, D. Y.; Chen, S.; Schmidt, C. Selective Axonal Growth of Embryonic Hippocampal Neurons according to Topographic Features of Various Sizes and Shapes. *Int. J. Nanomed.* **2010**, *6* (1), 45−57.

(14) Gomez, N.; Lee, J. Y.; Nickels, J. D.; Schmidt, C. E. Micropatterned Polypyrrole: A Combination of Electrical and Topographical Characteristics for the Stimulation of Cells. *Adv. Funct. Mater.* **2007**, *17* (10), 1645−1653.

(15) Gomez, N.; Chen, S.; Schmidt, C. E. Polarization of Hippocampal Neurons with Competitive Surface Stimuli: Contact Guidance Cues Are Preferred over Chemical Ligands. *J. R. Soc., Interface* **2007**, *4* (13), 223−233.

(16) Gomez, N.; Lu, Y.; Chen, S.; Schmidt, C. E. Immobilized Nerve Growth Factor and Microtopography Have Distinct Effects on Polarization versus Axon Elongation in Hippocampal Cells in Culture. *Biomaterials* **2007**, *28* (2), 271−284.

(17) Ferrari, A.; Cecchini, M.; Serresi, M.; Faraci, P.; Pisignano, D.; Beltram, F. Neuronal Polarity Selection by Topography-Induced Focal Adhesion Control. *Biomaterials* **2010**, *31* (17), 4682−4694.

(18) Wang, S.; Wan, Y.; Liu, Y. Effects of Nanopillar Array Diameter and Spacing on Cancer Cell Capture and Cell Behaviors. *Nanoscale* **2014**, *6* (21), 12482−12489.

(19) Wang, S.; Wang, H.; Jiao, J.; Chen, K.-J.; Owens, G. E.; Kamei, K.; Sun, J.; Sherman, D. J.; Behrenbruch, C. P.; Wu, H.; Tseng, H.-R. Three-Dimensional Nanostructured Substrates toward Efficient Capture of Circulating Tumor Cells. *Angew. Chem., Int. Ed.* **2009**, *48* (47), 8970−8973.

(20) Xie, X.; Xu, A. M.; Leal-Ortiz, S.; Cao, Y.; Garner, C. C.; Melosh, N. A. Nanostraw-Electroporation System for Highly Efficient Intracellular Delivery and Transfection. *ACS Nano* **2013**, *7* (5), 4351−4358.

(21) Chiappini, C.; Martinez, J. O.; De Rosa, E.; Almeida, C. S.; Tasciotti, E.; Stevens, M. M. Biodegradable Nanoneedles for Localized Delivery of Nanoparticles in Vivo: Exploring the Biointerface. *ACS Nano* **2015**, *9* (5), 5500−5509.

(22) Shalek, A. K.; Gaublomme, J. T.; Wang, L.; Yosef, N.; Chevrier, N.; Andersen, M. S.; Robinson, J. T.; Pochet, N.; Neuberg, D.; Gertner, R. S.; Amit, I.; Brown, J. R.; Hacohen, N.; Regev, A.; Wu, C. J.; Park, H. Nanowire-Mediated Delivery Enables Functional Interrogation of Primary Immune Cells: Application to the Analysis of Chronic Lymphocytic Leukemia. *Nano Lett.* **2012**, *12*, 6498−6504.

(23) Persson, H.; Køber, C.; Mølhave, K.; Samuelson, L.; Tegenfeldt, J. O.; Oredsson, S.; Prinz, C. N. Fibroblasts Cultured on Nanowires Exhibit Low Motility, Impaired Cell Division, and DNA Damage. *Small* **2013**, *9* (23), 4006−4016.

(24) Shalek, A. K.; Robinson, J. T.; Karp, E. S.; Lee, J. S.; Ahn, D.-R.; Yoon, M.-H.; Sutton, A.; Jorgolli, M.; Gertner, R. S.; Gujral, T. S.; MacBeath, G.; Yang, E. G.; Park, H. Vertical Silicon Nanowires as a Universal Platform for Delivering Biomolecules into Living Cells. *Proc. Natl. Acad. Sci. U. S. A.* **2010**, *107* (5), 1870−1875.

(25) VanDersarl, J. J.; Xu, A. M.; Melosh, N. Nanostraws for Direct Fluidic Intracellular Access. *Nano Lett.* **2012**, *12* (8), 3881−3886.

DOI: 10.1021/acsami.6b08668
ACS Appl. Mater. Interfaces 2016, 8, 23604−23613

(26) Xie, C.; Hanson, L.; Xie, W.; Lin, Z.; Cui, B.; Cui, Y. Noninvasive Neuron Pinning with Nanopillar Arrays. *Nano Lett.* **2010**, *10* (10), 4020−4024.
(27) Zhang, F.; Jiang, Y.; Liu, X.; Meng, J.; Zhang, P.; Liu, H.; Yang, G.; Li, G.; Jiang, L.; Wan, L. J.; Hu, J. S.; Wang, S. Hierarchical Nanowire Arrays as Three-Dimensional Fractal Nanobiointerfaces for High Efficient Capture of Cancer Cells. *Nano Lett.* **2016**, *16* (1), 766−772.
(28) Nagrath, S.; Sequist, L. V.; Maheswaran, S.; Bell, D. W.; Irimia, D.; Ulkus, L.; Smith, M. R.; Kwak, E. L.; Digumarthy, S.; Muzikansky, A.; Ryan, P.; Balis, U. J.; Tompkins, R. G.; Haber, D. a; Toner, M. Isolation of Rare Circulating Tumour Cells in Cancer Patients by Microchip Technology. *Nature* **2007**, *450* (7173), 1235−1239.
(29) Xie, X.; Xu, A. M.; Angle, M. R.; Tayebi, N.; Verma, P.; Melosh, N. Mechanical Model of Vertical Nanowire Cell Penetration. *Nano Lett.* **2013**, *13* (12), 6002−6008.
(30) Xie, X.; Aalipour, A.; Gupta, S. V.; Melosh, N. A. Determining the Time Window for Dynamic Nanowire Cell Penetration Processes. *ACS Nano* **2015**, *9* (12), 11667−11677.
(31) Aalipour, A.; Xu, A. M.; Leal-Ortiz, S.; Garner, C. C.; Melosh, N. A. Plasma Membrane and Actin Cytoskeleton as Synergistic Barriers to Nanowire Cell Penetration. *Langmuir* **2014**, *30* (41), 12362−12367.
(32) Berthing, T.; Bonde, S.; Rostgaard, K. R.; Madsen, M. H.; Sørensen, C. B.; Nygård, J.; Martinez, K. L. Cell Membrane Conformation at Vertical Nanowire Array Interface Revealed by Fluorescence Imaging. *Nanotechnology* **2012**, *23* (41), 415102.
(33) Hanson, L.; Lin, Z. C.; Xie, C.; Cui, Y.; Cui, B. Characterization of the Cell-Nanopillar Interface by Transmission Electron Microscopy. *Nano Lett.* **2012**, *12* (11), 5815−5820.
(34) Jahed, Z.; Molladavoodi, S.; Seo, B. B.; Gorbet, M.; Tsui, T. Y.; Mofrad, M. R. K. Cell Responses to Metallic Nanostructure Arrays with Complex Geometries. *Biomaterials* **2014**, *35* (34), 9363−9371.
(35) Wang, S.; Wang, H.; Jiao, J.; Chen, K. J.; Owens, G. E.; Kamei, K. I.; Sun, J.; Sherman, D. J.; Behrenbruch, C. P.; Wu, H.; Tseng, H. R. Three-Dimensional Nanostructured Substrates toward Efficient Capture of Circulating Tumor Cells. *Angew. Chem., Int. Ed.* **2009**, *48* (47), 8970−8973.
(36) Hai, A.; Shappir, J.; Spira, M. E. In-Cell Recordings by Extracellular Microelectrodes. *Nat. Methods* **2010**, *7* (3), 200−202.
(37) Robinson, J. T.; Jorgolli, M.; Park, H. Nanowire Electrodes for High-Density Stimulation and Measurement of Neural Circuits. *Front. Neural Circuits* **2013**, *7*, 38.
(38) Robinson, J. T.; Jorgolli, M.; Shalek, A. K.; Yoon, M.-H.; Gertner, R. S.; Park, H. Vertical Nanowire Electrode Arrays as a Scalable Platform for Intracellular Interfacing to Neuronal Circuits. *Nat. Nanotechnol.* **2012**, *7* (3), 180−184.
(39) Wong, S. Y.; Ulrich, T. a.; Deleyrolle, L. P.; MacKay, J. L.; Lin, J.-M. G.; Martuscello, R. T.; Jundi, M. a.; Reynolds, B. a.; Kumar, S. Constitutive Activation of Myosin-Dependent Contractility Sensitizes Glioma Tumor-Initiating Cells to Mechanical Inputs and Reduces Tissue Invasion. *Cancer Res.* **2015**, *75* (6), 1113−1122.
(40) Umesh, V.; Rape, A. D.; Ulrich, T. a.; Kumar, S. Microenvironmental Stiffness Enhances Glioma Cell Proliferation by Stimulating Epidermal Growth Factor Receptor Signaling. *PLoS One* **2014**, *9* (7), e101771−e101778.
(41) Ulrich, T.; de Juan Pardo, E. M.; Kumar, S. The Mechanical Rigidity of the Extracellular Matrix Regulates the Srtucture, Motility, and Proliferation of Glioma Cells. *Cancer Res.* **2009**, *69* (10), 4167−4174.
(42) Persson, H.; Li, Z.; Tegenfeldt, J. O.; Oredsson, S.; Prinz, C. N. From Immobilized Cells to Motile Cells on a Bed-of-Nails: Effects of Vertical Nanowire Array Density on Cell Behaviour. *Sci. Rep.* **2015**, *5*, 18535.
(43) Louis, D. N. Molecular Pathology of Malignant Gliomas. *Annu. Rev. Pathol.: Mech. Dis.* **2006**, *1*, 97−117.
(44) Bellail, A. C.; Hunter, S. B.; Brat, D. J.; Tan, C.; Van Meir, E. G. Microregional Extracellular Matrix Heterogeneity in Brain Modulates Glioma Cell Invasion. *Int. J. Biochem. Cell Biol.* **2004**, *36* (6), 1046−1069.
(45) Agudelo-Garcia, P. A.; De Jesus, J. K.; Williams, S. P.; Nowicki, M. O.; Chiocca, E. A.; Liyanarachchi, S.; Li, P.; Lannutti, J. J.; Johnson, J. K.; Lawler, S. E.; Viapiano, M. S. Glioma Cell Migration on Three-Dimensional Nanofiber Scaffolds Is Regulated by Substrate Topography and Abolished by Inhibition of STAT3 Signaling. *Neoplasia* **2011**, *13* (9), 831−840.
(46) Kim, D.-H.; Provenzano, P. P.; Smith, C. L.; Levchenko, A. Matrix Nanotopography as a Regulator of Cell Function. *J. Cell Biol.* **2012**, *197* (3), 351−360.
(47) Mofrad, M. R. K., Kamm, R. D., Eds.; *Cellular Mechanotransduction: Diverse Perspectives from Molecules to Tissues*; Cambridge University Press, 2014.

DOI: 10.1021/acsami.6b08668
ACS Appl. Mater. Interfaces 2016, 8, 23604−23613